Full field-of-view imaging and multistatic operations for SuperDARN Borealis radars

R.A. Rohel[1], P. Ponomarenko[1], and K.A. McWilliams[1]

[1]University of Saskatchewan, Saskatoon, Canada

Key Points:

- We developed wide-beam transmission to probe an entire SuperDARN field of view simultaneously and to enable bistatic operations
- New multistatic operation of SuperDARN radars provides additional measured velocity vector components
- New wide-beam and multistatic operations significantly improve temporal resolution and spatial coverage by SuperDARN

Corresponding author: Pasha Ponomarenko, pasha.ponomarenko@usask.ca

Abstract

Super Dual Auroral Radar Network (SuperDARN) consists of more than 30 monostatic high-frequency (HF, 10-18 MHz) radars which utilise signals scattered from decameter-scale ionospheric irregularities for studying dynamic processes in the ionosphere. By combining line-of-sight velocity measurements of ionospheric scatter echoes from radars with overlapping fields of view, SuperDARN provides maps of ionospheric plasma drift velocity over mid and high latitudes. The conventional SuperDARN radars consecutively scan through sixteen beam directions with dwelling time of 3.5 s/beam, which places a lower limit of one minute to sample the entire field of view. In this work we remove this limitation by utilizing advanced capabilities of the recently developed Borealis digital SuperDARN radar system. Combining a wide transmission beam with multiple narrow reception beams allows us to sample all conventional beam directions simultaneously and to increase the sampling rate of the entire field of view by up to sixteen times without noticeable deterioration of the data quality. The wide-beam emission also enabled the implementation of multistatic operations, where ionospheric scatter signals from one radar are received by other radars with overlapping viewing areas. These novel operations required the development of a new model to determine the geographic location of the source of the multistatic radar echoes. Our preliminary studies showed that, in comparison with the conventional monostatic operations, the multistatic operations provide a significant increase in geographic coverage, in some cases nearly doubling it. The multistatic data also provide additional velocity vector components increasing the likelihood of reconstructing full plasma drift velocity vectors.

Plain Language Summary

The Super Dual Auroral Radar Network (SuperDARN) consists of more than 30 high-frequency (HF, 10-18 MHz) radars that observe the ionized part of the Earth's atmosphere to study Space Weather phenomena, like magnetic storms and the aurora. Each SuperDARN radar transmits a radio wave at a particular frequency and receives the returns scattering from ionized structures. The returns are analyzed to extract information about processes in near-Earth space. Conventionally, these radars scan 16 azimuthal directions consecutively, dwelling for 3.5 s in each direction, which limits the sampling rate of the field-of-view to one minute. In this work, we use a recently developed digital SuperDARN radar system called Borealis to improve the sampling rate by an order of magnitude by illuminating the whole field of view with a broad transmitter beam and receiving radar returns from all 16 directions simultaneously using narrow receiver beams. We also implemented a technique to receive signals sent from one radar by other radars with overlapping viewing areas. This provides a significant increase (nearly doubles) the geographic area of coverage, compared with using the same radar for both transmission and reception.

1 Introduction

The Super Dual Auroral Radar Network (SuperDARN) is a collection of high frequency (HF, 10-18 MHz) phased-array radars across the globe that collectively monitor space weather conditions and plasma convection in the mid- and high-latitude ionosphere (Greenwald et al., 1995; Chisham et al., 2007; Nishitani et al., 2019). The radars emit multiple-pulse sequences that are $\simeq 0.1$ s in duration. The radars combine received samples in such a way that autocovariance functions (ACF) are formed for each of 70-100 range gates, which are separated by 45 km in group range along a given azimuthal direction (beam). A conventional SuperDARN radar uses 16 beams separated by 3-4° (currently 3.24°) in azimuth to form the radar field-of-view (FOV), covering $\simeq 50°$ in azimuth. The ACFs are normally produced by averaging 30 to 35 multi-pulse sequences (N_a), which corresponds to an effective integration (beam-dwell) time, t_i, of 3-3.5 s.

Analysis of SuperDARN ACF data is performed using a conventional software package known as the Radar Software Toolkit (RST) (SuperDARN Data Analysis Working Group, 2021). RST fits model functions to the ACF envelope ('power') and ACF phase to estimate the signal-to-noise (SNR) ratio, the line-of-sight (LOS) velocity component, the spectral width and the respective measurement errors (for more detail see, e.g, Ponomarenko & Waters, 2006). Measurements from radars with overlapping FOVs are used to generate plasma drift velocity vector fields. Functional fitting is used to create global-scale plasma velocity maps from the combined measured velocity components observed by multiple radars (Ruohoniemi & Baker, 1998; Fiori et al., 2010; Bristow et al., 2022). These are equivalent to global-scale maps of electric potential at high latitudes.

SuperDARN has been successfully recording data from the high-latitude ionosphere for three decades. Its original operation regime, in which a narrow beam scans through 16 adjacent directions over the course of 1-2 min, remains essentially unchanged. Ideally, the full FOV should be scanned at one time, so that the signals from all beam directions can be recorded simultaneously. The hardware accessible at the inception of SuperDARN did not allow for this approach. The conventional sweep of the FOV proved to be successful for scientific discovery and has continued to be used. At the time of writing, a 16-beam scan is completed within one minute. The one-minute scan defines the sampling rate of the full FOV. The integration time along a beam direction is equal to only one sixteenth of the sampling rate, i.e., $t_i \simeq$3.5 s per beam. Because the statistical variability of a radar signal decreases proportionally to $1/\sqrt{t_i}$ (e.g., Bendat & Piersol, 2010), the mismatch between the FOV sampling period and the integration time leads to a four-fold increase in statistical errors. Another undesirable effect of consecutive beam scanning is that different beams within a single scan are sampled at different times, with the time offset ranging from 3.5 s between the adjacent beams to up to one minute for the beams at the opposite edges of the FOV. While the majority of SuperDARN radars have been built in pairs with significantly overlapping FOVs, limitations on timing accuracy between the radar sites made bistatic operations virtually unexploited, except for recent proof-of-concept work by Shepherd et al. (2020).

SuperDARN radars benefit from the HF radio wave's ability to propagate over-the-horizon through consecutive "hops" between the ionosphere and the ground surface. At a fixed working frequency this propagation mechanism limits the range coverage to one or two bands of ionospheric scatter, separated by echoes from the ground surface (see, e.g., middle panel in Figure 1 from Ponomarenko et al., 2008). The location of these bands relative to the radar changes significantly with varying ionospheric conditions, e.g., between higher daytime and lower nighttime ionospheric plasma density. SuperDARN uses an empirical statistical model of ionospheric velocity distribution to fill gaps in radar coverage (e.g., Ruohoniemi & Baker, 1998; Cousins & Shepherd, 2010; Thomas & Shepherd, 2018). The range coverage can be improved, in principle, by applying multi-frequency sounding, but under the conventional operational regime this is accomplished through interleaving scans at different frequencies, which decreases the sampling rate at a particular frequency in proportion to the number of frequencies being used.

Since the start of the SuperDARN collaboration, to improve the performance of their radars, some participating groups have designed their own hardware that differs from the original design. For example, the University of Leicester SuperDARN group took advantage of SuperDARN's low duty cycle and developed the "Stereo" SuperDARN radar system, by adding a second receiver system to the existing conventional-style transmitter/receiver system. Stereo radars transmit back-to-back pulses at two distinct frequencies and receive the echoes using separate receiver hardware for each frequency band (i.e., on separate receiver channels) (Lester et al., 2004). They are capable of operating using different scanning patterns with each channel, e.g., one channel can perform a conventional 16-beam sweep while the other channel samples a single beam at a higher rate (the so-called "camping" beam).

Another feature of conventional SuperDARN radars that can be improved relates to data loss during the automatic beamforming and data averaging done at the radar site. The initial data samples normally are not preserved, which prohibits adaptive post-processing. Such an approach was originally dictated by the limited data storage capabilities available in the early 1990s. As more extensive data storage became available, Yukimatu and Tsutsumi (2002) developed a system to record complex in-phase and quadrature (I&Q) voltage samples, in the first step towards flexible data post-processing. The next major development in this direction was made by the SuperDARN team at the University of Alaska, Fairbanks (UAF), where the first SuperDARN system using software-defined radios (SDRs) was designed. This moved both transmitter waveform generation and receiver sampling into the digital domain, allowing for active receiver beamforming as a prerequisite for flexible sampling of the FOV. The UAF system also enabled the receivers to sample a wide frequency band, providing a basis for simultaneous multi-frequency operations (Parris, 2003). The most recent advancements in addressing the above issues has been achieved at the University of Saskatchewan through development of a new SDR-based digital radar system Borealis (McWilliams et al., 2023).

In the present work, we exploit Borealis' advanced capabilities to remove limitations imposed by the conventional systems and their operational regime without altering the quality of the data products in any significant way. This is achieved by introducing wide-beam transmission modes that enable simultaneous (multi-beam) measurements across the entire radar FOV. In addition to the conventional monostatic SuperDARN application, the wide-beam emission is applied to a bistatic radar configuration to produce an additional set of LOS velocity measurements along a new set of directions. Besides providing an independent set of LOS measurements, the bistatic capability improves the spatial coverage of SuperDARN thus decreasing the reliance on the statistical models and increasing the role of the actual data in generating high-latitude plasma circulation maps.

2 SuperDARN Operations: Comparing Conventional SuperDARN and Borealis Radars

2.1 Conventional SuperDARN System

Each SuperDARN radar is equipped with a main transmit-receive array of 16 evenly-spaced log-periodic or twin-terminated folded dipole (TTFD) antennas (Greenwald et al., 1995; Sterne et al., 2011). At most sites, the main antenna array is also accompanied by a receive-only auxiliary interferometer array consisting of four antennas used to determine the vertical angle of arrival (elevation angle) of the signal.

The conventional SuperDARN radar system was designed primarily with analog radar hardware (Greenwald et al., 1985). In the original design, frequency synthesizers generate a sine-wave signal at the desired frequency. This signal is fed into a phasing matrix representing a tree of divider/combiner and delay-line elements that collectively split the input signal into 16 distinct output signals. The output signals are amplified individually and routed to the respective antennas using a linear time delay progression across the array so that the relatively narrow main lobe of the array (the transmitted beam) is pointing in the desired direction.

The radar echoes returning from the ionosphere and/or ground surface are received by the antennas and routed back to the phasing matrix. At this stage, the matrix acts as a combiner and delay-line, first applying a delay to each input signal before coherently adding the signals. The linear delay progression across the antenna array is identical for both transmission and reception, thereby providing optimal operation through matching transmit and receive beam patterns. This results in SuperDARN's high sensitivity in a narrow beam direction.

2.2 Borealis SuperDARN System

The Borealis radar system provides more operational and data processing flexibility than the conventional SuperDARN system (McWilliams et al., 2023). Borealis uses 16 software-defined radios (SDRs) to control transmission and reception for each antenna individually, eliminating the need for analog phasing matrices and analog filtering of signals. This allows for antenna-level control that the conventional SuperDARN systems do not have. The Borealis system can operate with arbitrary waveforms within a 5 MHz band, enabling multi-frequency operations. The Borealis system is capable of controlling the frequency and timing of signals from any given antenna and the relative phases between antennas, thereby eliminating the linear phase limitation imposed by the conventional phasing matrix. The signal amplification and transmit/receive switching is handled separately from the SDRs, and in this respect Borealis does not differ from the conventional system. Transmitter hardware at SuperDARN Canada radars includes automatic gain control circuitry that tunes the output power to a calibrated value, disabling any power modulation.

For signal reception, the SDRs filter the received signal into a 5 MHz band around a specified center frequency and then mix and downsample it. The controlling computer records samples from each SDR independently. The typical Borealis processing chain uses staged filtering and downsampling to produce samples at the same rate as the conventional system, but for each antenna individually. Beamforming can be done with arbitrary phase offsets applied to each antenna, as opposed to the more limited linear phase progression across the array in the conventional systems. Since the samples for each antenna are preserved, the data can be post-processed with any desired method. In the work presented in this paper, as an example, 16 narrow receiver beams are created from the same dataset in post-processing to sample the 16 conventional SuperDARN receiver directions simultaneously.

3 Extending Operational Capabilities

In their initial operations, the Borealis systems were configured to operate in the same way as the conventional SuperDARN radars, so as not to disrupt the continuity of the global dataset. Here we describe how the extended capabilities of Borealis system are being developed to remove some of the limitations of the conventional SuperDARN system while still maintaining the common requirements of the global dataset. On the transmitter side, we utilize the ability to apply an arbitrary phase distribution along the antenna array so that the transmission occurs within a wide beam illuminating the entire conventional FOV. On the receiver side, we utilize the ability to store received signals from individual antennas to beamform multiple simultaneous received beam directions. This allows us to sample 16 beam directions simultaneously, increasing the respective sampling rate 16-fold without significant deterioration of data quality. We apply the wide-beam transmission mode to a multistatic setup, where signals emitted from one radar site are scattered by the ionospheric irregularities and received at other sites. The wide-beam emission eliminates the spatio-temporal limitations imposed by the conventional consecutive narrow-beam scanning, thereby making it possible to sample the entire multistatic FOV simultaneously. When bistatic sounding is limited to the common viewing area of a narrow transmit and a narrow receive beam, the overlap is effectively a single range gate for each integration time. To accurately locate multistatic scatter echoes throughout a large FOV, we developed a new bistatic geolocation model for high latitudes.

3.1 Wide-Beam Operations

3.1.1 Beamforming Principles

With the Borealis system, a set of received signals from the antennas can provide beamformed data from multiple directions measured simultaneously (McWilliams et al., 2023). This allows for azimuthal mapping of signal sources consistent with the conventional SuperDARN narrow-beam operations. Importantly, the simultaneous multi-directional reception is only feasible if a sufficient amount of power is being radiated in all directions of interest to provide an acceptably high SNR. In radar systems, uniform transmission over a wide area is typically achieved with a combination of amplitude and phase modulation across the antennas of the array. The simplest way to illuminate a conventional SuperDARN FOV of ± 24.3 from the boresight direction is to transmit only on one or two antennas without phase offset, as demonstrated in, e.g, McWilliams et al. (2023). This amounts to an amplitude modulation across the array using a binary window. With any amplitude modulation the total power output of the array is reduced, so it is advantageous to apply phase-only modulation and maximize the total radiated power. Each SuperDARN Canada antenna has conventional transmitter hardware and is only able to be either transmitting at full power or switched off, which makes power modulation suboptimal. Thus, a phase-only modulation scheme was investigated in the work presented here.

Using the method of Boeringer et al. (2005), we generated transmission patterns that radiated across the entire conventional SuperDARN FOV. In searching for well-performing solutions, to reduce the parameter space the following restrictions were applied:

1. the phase progression across the array must be symmetric with respect to the boresight direction,
2. the outermost antennas are set to a reference phase of 0 radians, and
3. all phases must lie between 0 and 2π radians.

The main lobe width for transmission was restricted to $\pm 24.3^\circ$ from the boresight direction to cover the conventional SuperDARN FOV. Various combinations of peak to side lobe ratio, main lobe ripple, and transition width between the main lobe and side lobes were investigated to find suitable beam patterns. Optimal phase progressions were found for all common SuperDARN Canada operating frequencies and simulated using Numerical Electromagnetics Code (NEC) 2. In the simulation, we used twin-terminated folded dipole antennas with a reflective screen placed behind the array (Sterne et al., 2011). Optimized gain patterns for several array configurations at 10.8 MHz are shown in panel (a) of Figure 1. The array configurations include the conventional narrow-beam pattern (purple) as well as optimal wide-beam patterns using 2, 8 and 16 antennas (green, orange and blue lines, respectively). Panel (b) depicts the phase progression across the array for the same configurations, with the narrow-beam phases (purple) arbitrarily shifted up by π radians to disambiguate from the 2-antenna phase progressions (green).

On November 7, 2022, we ran an interleaved experiment to compare the three wide-beam modes illustrated in Figure 1. Every 3.7 s the operation mode was switched between 16-antenna, 8-antenna, and 2-antenna transmission, resulting in a temporal resolution of 11.1 s for each mode. To compare the relative SNR of each mode, we limited the analysis to range gates where all modes had valid data during their adjacent integration times. Figures 2(a) and 2(b) are the two-dimensional histogram of SNR values for these points from the arbitrarily chosen beam 12 direction. These data were post-processed with conventional beamforming for beam 12 such that a narrow beam with peak sensitivity at 14.6° clockwise of boresight was formed. The 16-antenna mode is compared to the 2-antenna mode in Figure 2(a), and the 8-antenna mode is compared to the 2-antenna mode in Figure 2(b). A consistent offset in SNR is present in both panels. That offset is approximately 9 dB for Figure 2(a) and 6 dB for Figure 2(b).

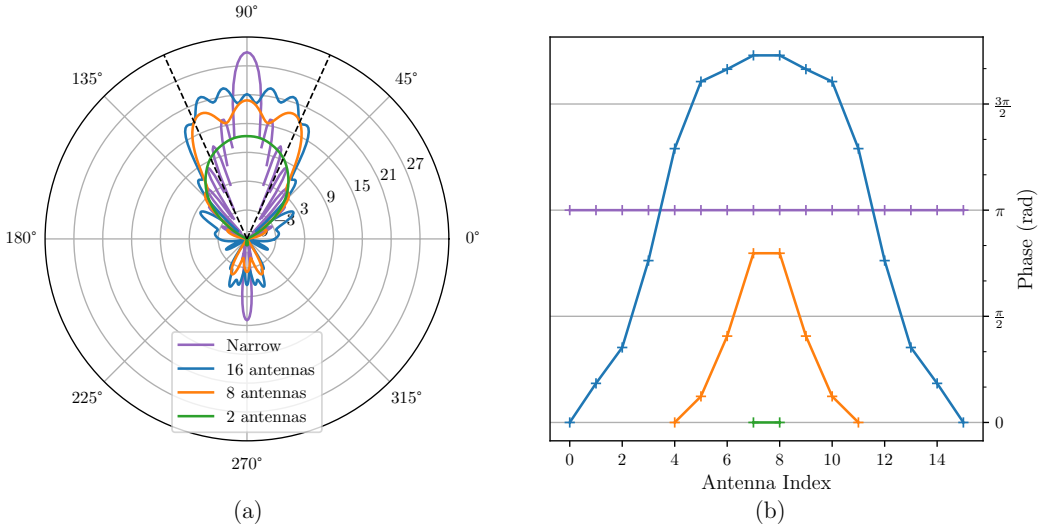

Figure 1: (a) Directivity in dB relative to an isotropic source at an elevation angle of 35° for 16-antenna (blue), 8-antenna (orange), and 2-antenna (green) wide-beam modes, as well as for the conventional 16-antenna narrow-beam mode (purple). (b) Phase progressions across the antenna array used to generate the patterns in (a). The phase progression for the conventional pattern has been shifted up by π rad to distinguish from the phase progression for the 2-antenna mode.

While the histograms contain data from beam 12 only, Figure 2(c) includes the average SNR as a function of beam direction, which was determined for all data points satisfying the selection criteria. Of note in this figure is the dependence of average signal SNR on beam direction compared to that predicted by the simulation in Figure 1. One can see that the 2-antenna pattern agrees well between these two figures, with similar and relatively low SNR across the FOV, but with slightly higher SNR on the left side of the FOV. The 16-antenna and 8-antenna patterns also contain some of the characteristics of Figure 1(a), but with generally higher SNR on the left side compared to the right side. The three-lobe pattern of the 8-antenna mode can clearly be seen, as well as the dip in 16-antenna SNR at boresight (90°). The SNR difference between right and left for the three modes is likely due to spatially non-uniform ionospheric scatter conditions during the two hours of this experiment.

An important consideration with wide-beam transmission modes is their impact on signals received through receiver side lobes. For conventional SuperDARN beam patterns, the maximum directivity of the first side lobe is approximately 13 dB less than the peak directivity of the main lobe. During conventional operations, the colocated transmit and receive beams have the same shape and point in the same direction, which results in a 26 dB difference in directivity between the main lobe and first side lobe. With wide-beam transmission, there is no significant difference in directivity across the FOV, resulting in a $\simeq$13 dB difference in directivity between the main lobe and first side lobe of the receiver antenna pattern. Since SuperDARN regularly receives signals with SNR above 30 dB, during wide-beam transmission modes it is therefore more likely to receive large-SNR signals from undesirable directions through the received side lobes.

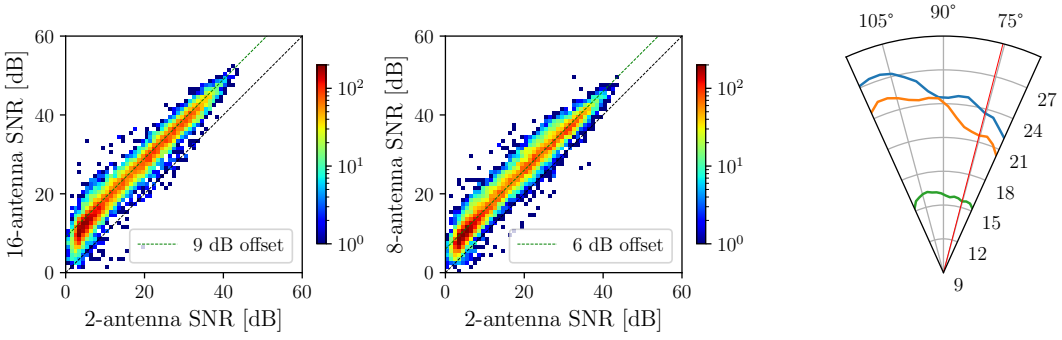

Figure 2: (a) and (b): Two-dimensional histograms of SNR from beam 12 comparing wide-beam methods. In (a), the vertical axis denotes the SNR level detected using the 16-antenna mode, and the horizontal axis denotes the SNR level detected using the 2-antenna mode. Panel (b) shows the same, but with the 8-antenna mode on the vertical axis. Green lines denote the SNR offset expected purely based on the number of transmitting antennas, and black lines denote equal SNR. (c) Mean SNR in dB for all shared points as a function of azimuthal direction for 16-antenna (blue), 8-antenna (orange), and 2-antenna (green) wide-beam modes. The thin red line denotes the center of beam 12.

3.1.2 Wide-Beam Data

Figure 3 contains time-range plots of SNR (panels a-c), LOS velocity (d-f), and spectral width (g-i) along beam 7 during the November 7 test of three wide-beam modes (23:00-00:00 UTC) and the regular operations following the experiment (00:00-01:00 UTC). The radar was transmitting at 10.8 MHz. During the wide-beam operations we applied interleaved sampling by consecutively switching between three wide-beam modes every 3.7 s. The left, middle and right columns correspond to 2- 8- and 16-antenna wide-beam operations, respectively. After 00:00 UTC we used a conventional SuperDARN two-frequency sounding mode, called *twofsound*, during which the radar switches back and forth between the two operating frequencies of 10.8 and 12.0 MHz in each successive scan. For compatibility with the wide-beam observations, only data from the same frequency (10.8 MHz) are shown in Figure 3. The most prominent feature of Figure 3 is the difference in temporal resolution before and after 00:00 UTC. In this particular case, the wide-beam operation provides an order of magnitude improvement in the sampling rate. Each beam is sampled every 11.1 s in wide-beam operations, while the two-frequency mode provides samples only every 2 min. In the wide-beam mode, the temporal resolution for all beams is limited by the integration time rather than by the FOV scan duration. For conventional operations, the same temporal resolution can only be achieved by continuous sampling one single beam, i.e., at the expense of the data from all other beam directions. This improvement has been demonstrated in Figure 6 from (McWilliams et al., 2023) in a proof-of-concept study with a 2-antenna wide-beam transmission pattern.

As one would expect, the widening of the emission beam leads to a decrease in the echo signal power and therefore also in the SNR. For the wide-beam emission, one would expect some reduction in spatial coverage, as the SuperDARN data pre-selection is based on SNR (Ponomarenko et al., 2022). This effect is particularly evident in the 2-antenna data (right column in Figure 3), which exhibits a noticeable increase in SNR and spatial coverage after switching to the conventional operations using all antennas after 00:00 UTC. In this case, the average SNR should change by $\simeq 18$ dB (Figure 1(a). In contrast, such sharp transitions are nearly undetectable for the 8- and 16-antenna wide-beam modes (left and middle columns in Figure 3). For these modes the expected drop in SNR be-

comes comparable to the statistical fluctuations of the echo power. The magnitude of the power fluctuations σ_P is defined as:

$$\sigma_P = \frac{P}{\sqrt{N_a}} \tag{1}$$

where P is the signal power (e.g., Bendat & Piersol, 2010). In our case, $N_a \simeq 35$ so the relative variations in power would be equivalent to $\simeq 7-8$ dB while the drop in SNR according to Figure 1(a) is $\simeq 8-10$ dB.

In summary, the wide-beam mode provides simultaneous sampling of all beam directions with relatively little effect on the data quality when 8 and 16 antennas are used to transmit a wide-beam to fill the conventional SuperDARN FOV. Compared to the conventional operation mode (integration time $\simeq$3.5 s per beam with 1 min FOV scan duration), this new capability makes it possible either to increase the sampling rate by up to 16 times or to decrease the statistical variability by up to $\sqrt{16} = 4$ times. When decreasing statistical variability by increasing the integration time, one needs to take care not to exceed the stationarity interval (e.g., Bendat & Piersol, 2010) after which further increases in the number of averages (integration time) would not improve the situation. In general, a trade-off between the sampling rate and the acceptable level of statistical errors needs to be established based on the scientific objectives of a given operation mode.

3.2 Multistatic Operations

3.2.1 Monostatic vs Bistatic Basics

The primary parameter measured by SuperDARN radars is the Doppler velocity component determined from the observed Doppler frequency shift f_D of an ionospheric echo. A general expression for f_D is given by the following:

$$f_D = \frac{1}{2\pi}\vec{K}\cdot\vec{V} \tag{2}$$

where $\vec{K} = \vec{k_r} - \vec{k_t}$ is the scatter vector representing the difference between the received $\vec{k_r}$ and transmitted $\vec{k_t}$ wave vectors at the scatter point, while $\vec{V}$ is plasma drift velocity vector at the scatter location. Equation 2 can be rewritten as:

$$f_D = \frac{2V}{\lambda}\cos\delta\cos(\theta/2) \tag{3}$$

where θ is the angle between $\vec{k_r}$ and $\vec{k_t}$, and δ is the angle between $\vec{K}$ and $\vec{V}$ and λ is the radar emission wavelength in the medium (e.g., Willis, 2005).

Following the Booker-Gordon theory (H. Booker & Gordon, 1950) applied to field-aligned irregularities (H. G. Booker, 1956), a wave encountering such irregularities is scattered into a cone of equal aspect angle relative to the magnetic field (see, e.g., Figure 2 from Galushko et al., 2013). In other words, the scattering is specular with respect to the magnetic field lines. This corresponds to the scatter vector being perpendicular to the magnetic field:

$$\vec{K}\cdot\vec{B} = 0. \tag{4}$$

When it comes to radio wave scattering, there are important differences between monostatic and bistatic radar configurations.

1. In the monostatic case, both $\vec{k_t}$ and $\vec{k_r}$ lie in a plane perpendicular to $\vec{B}$ and are antiparallel to each other. In the bistatic configuration they are not necessarily orthogonal to $\vec{B}$ provided that the condition described by Equation 4 is satisfied.
2. In the bistatic case, $\vec{K}$ at the scattering location is aligned with the bisector of the angle between the LOS directions from the receiver and transmitter sites.
3. The magnitude of the scatter vector in the bistatic case can vary between $2k$ (backscatter, $\vec{k_r} \uparrow\downarrow \vec{k_t}$) and 0 (forward scatter, $\vec{k_r} \uparrow\uparrow \vec{k_t}$).

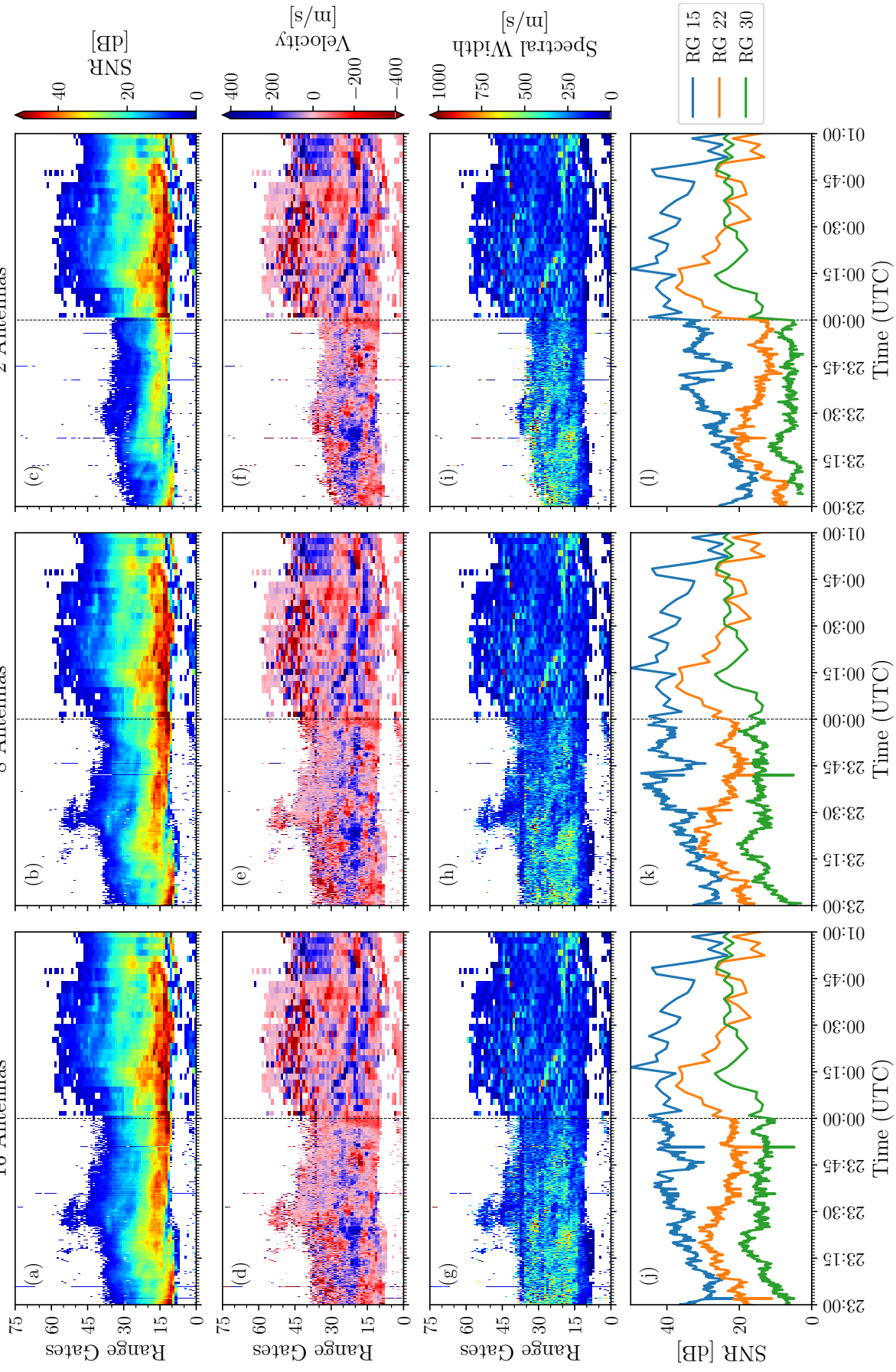

Figure 3: Comparison of wide-beam transmission patterns (23:00-00:00 UTC) with those for conventional SuperDARN operations (00:00-00:01 UTC) along beam 7 of Inuvik radar on 07-08 November 2022. Top three rows show time-range gate maps for SNR, Doppler velocity, and spectral width, respectively. The bottom row show dependence of SNR vs UTC in selected range gates. The first (panels a, d, g and j), second (b, e, h, k) and third (c, f, i, and l) columns correspond to 16-, 8- and 2-antenna wide-beam transmissions before 00:00 UTC, respectively. Blue, orange and green lines in the bottom row (panels j, k, and l) show SNR at range gates 15, 22, and 30, respectively.

3.2.2 Bistatic Geolocation Principles

This work is not the first instance of SuperDARN radars being used in a bistatic configuration. Shepherd et al. (2020) observed three propagation modes using a pair of mid-latitude SuperDARN radars, namely direct propagation between transmitter and receiver radars, single-hop scatter from the ground surface, and half-hop scatter from the ionosphere. Perry et al. (2017) investigated the transionospheric propagation of SuperDARN signals transmitted from Saskatoon and received by a passing satellite. Perry et al. (2017) investigated only direct-path signals, but they noted evidence of multipath propagation through the ionosphere. In their bistatic investigation, Shepherd et al. (2020) looked only at symmetric SuperDARN beams, where the propagation distance from the transmitter to the scattering location and from the scattering location to the receiver was equal. Shepherd et al. (2020) observed scatter from ionospheric irregularities, but the use of narrow beams for both transmission and reception limited the spatial extent of these observations to the region where the beams overlapped, i.e., effectively to a single range gate per integration time. With the Borealis system, wide-beam transmission patterns and multi-beam reception can be used to observe simultaneous bistatic scatter over much larger spatial extents.

The existing SuperDARN geolocation algorithms are developed for a monostatic radar (Chisham et al., 2008). We have derived a method for locating scatter in a bistatic configuration. This method is based on several assumptions:

1. The Earth is spherical over the wave path.
2. The ionosphere is stratified only radially (vertically with respect to the Earth surface), such that there are no horizontal gradients in the background electron density.
3. The geomagnetic field is oriented radially, which represents a reasonable approximation at the high latitudes covered by the SuperDARN Canada radars.

The propagation geometry for bistatic signals is shown schematically in Figure 4. For simplicity, a "flat Earth" geometry is drawn. This does not affect the physics of radio wave scattering on a curved Earth, which we discuss in relation to the simplified diagram. The signal is transmitted at some elevation angle ε and refracts in the ionosphere before being scattered by ionospheric irregularities. As mentioned in Subsection 3.2.1, at the scatter point, the angle between the magnetic field $\vec{B}$ and the incident wave vector $\vec{k_t}$ is equal to the angle between $\vec{B}$ and the scattered wave vector $\vec{k_r}$. For direct forward propagating signal, the signal strikes the ground at the tip of the blue arrow. This path is equivalent to one-way single-hop ground scatter in the monostatic radar case.

The assumption about the vertical magnetic field represents a reasonable approximation for high-latitude SuperDARN radars. In this case, the magnetic field line passing through the scatter point can be considered as a hinge around which the remaining part of the downward ray trajectory is rotated, creating a ground projection of the scatter cone. For a vertical (radial) magnetic field orientation, the scattered radiation creates a circle of illumination on the ground (red dashed line in the horizontal plane in Figure 4), which greatly simplifies the ground range calculation. Note that a similar illustration of the described above "hinge" principle can be found in Figure 5 from Borisova et al. (2002).

Using the theorem of Breit and Tuve (Davies, 1965) as an approximation, one can simplify the bistatic geolocation problem to the geometry depicted in Figure 5(a). This figure shows the actual path from Figure 4 in blue, and the straight-line virtual path in dark green. Since the straight-line virtual propagation path is fixed for a given group range and initial elevation angle, the actual scattering location can be ignored. Instead, the total geocentral arc spanned by the wave can be derived, based solely on the group range and the elevation angle measurements.

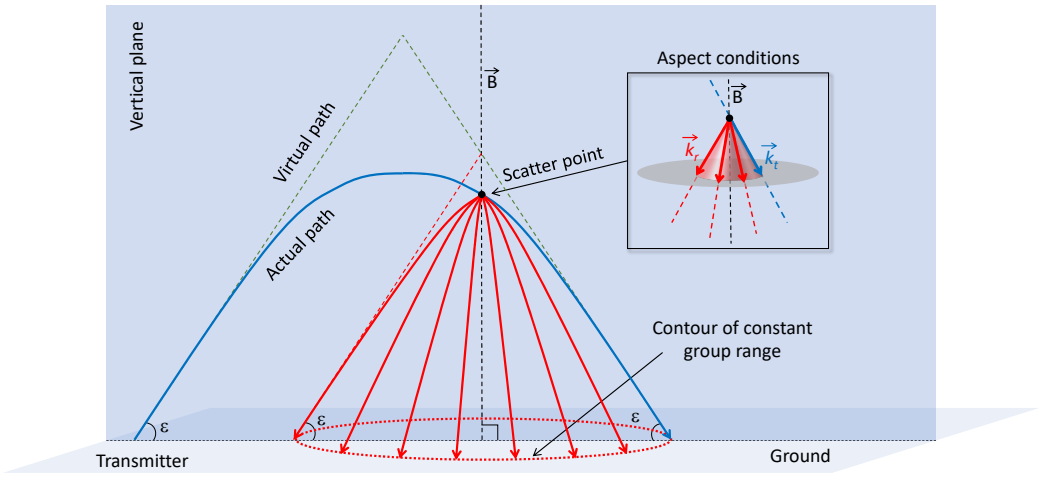

Figure 4: Schematic illustration of aspect conditions' effect on bistatic scatter geometry (see text for details).

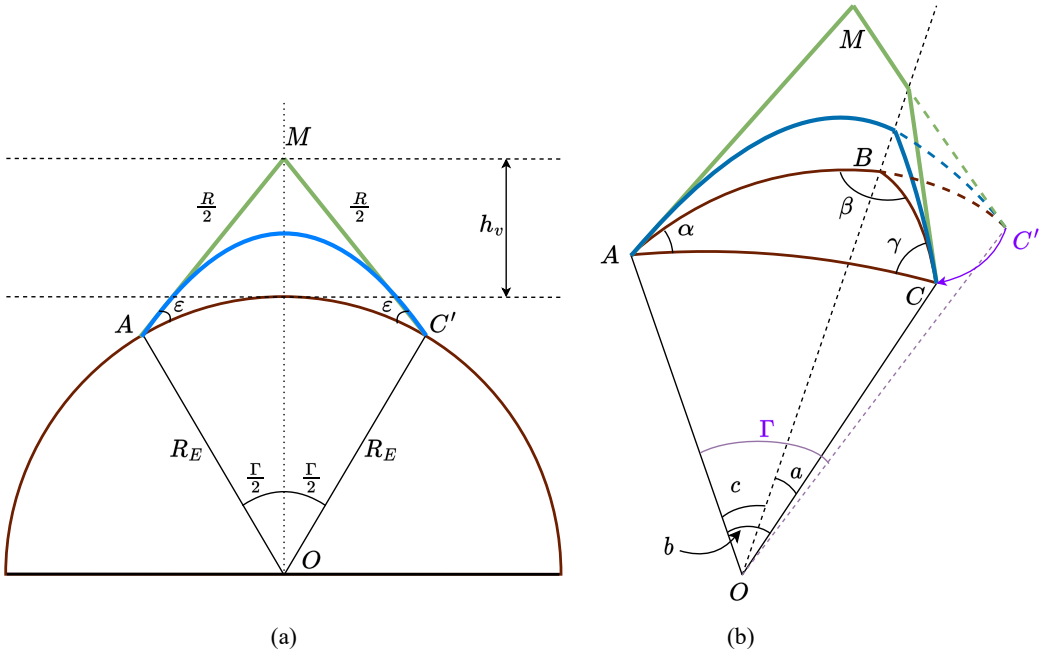

Figure 5: (a) Simplified geometry for determining geocentral arc traversed by HF propagation. Blue is the actual ray path in the medium, and dark green is the equivalent straight line path in vacuum. (b) Transmitter site A, receiver site C, and projection of scatter point on Earth's surface B. Brown lines denote great-circle arcs along the surface of Earth.

Following the work of Thomas and Shepherd (2022), for example, the virtual height of the midpoint of the path for a spherical Earth can be written as

$$h_v = \sqrt{\frac{R^2}{4} + R_E^2 + RR_E \sin\varepsilon} - R_E, \tag{5}$$

where R is the group path calculated as the time of flight Δt multiplied by the speed of light in a vacuum c, $R = \Delta tc$, and R_E is the Earth's radius.

Next, one can use the virtual height of the midpoint M in the sine law for planar triangles to find the geocentral angle Γ for single-hop propagation.

$$\Gamma = 2\arcsin\left(\frac{R}{2}\frac{\cos\varepsilon}{R_E + h_v}\right) \tag{6}$$

From there, one must consider the spherical triangle formed by the Transmitter-Scatterer-Receiver (ABC) journey, depicted in Figure 5(b). One can measure γ, which is the angle $\angle BCA$, by the beam's azimuthal angle at the receiver and the fixed location of the transmitting and receiving sites. One also knows that the total geocentral angle traversed on the journey is Γ, which is the sum of the geocentral angles $c = \angle AOB$ and $a = \angle BOC$. One can then relate

$$a = \Gamma - c \tag{7}$$

and insert this into the spherical triangle cosine law with some rearrangements to find

$$c = \arctan\left[\frac{1 - \cos(b)\cos(\Gamma) - \sin(b)\sin(\Gamma)\cos(\gamma)}{\cos(b)\sin(\Gamma) - \sin(b)\cos(\Gamma)\cos(\gamma)}\right] \tag{8}$$

From here, there is enough information to solve for all other angles and lengths in the system. The virtual height at both the receiver, h_{rx}, and transmitter, h_{tx}, can be calculated using the geocentral arc spanning each leg of the journey. This is a simple sine law application, yielding

$$h_{rx} = R_E\left(\frac{\cos(\varepsilon)}{\cos(a + \varepsilon)} - 1\right) \tag{9}$$

and

$$h_{tx} = R_E\left(\frac{\cos(\varepsilon)}{\cos(c + \varepsilon)} - 1\right). \tag{10}$$

These virtual heights are equal to each other only when $a = c$, i.e., the transmit and receive ray paths are equal.

It is important to note that this geolocation algorithm represents a generalization of a monostatic case. To illustrate that this is the case, the transmitter-to-receiver geocentral angle b should be set to zero. Equation 8, through the half-angle tangent formula, then reduces to

$$c = \arctan\left[\frac{1 - \cos(\Gamma)}{\sin(\Gamma)}\right] = \frac{\Gamma}{2}. \tag{11}$$

This result is consistent with the half-hop monostatic geometry, since a back-scattered radio wave must retrace its outbound trajectory to be received by the transmitting radar. The geocentral angle from the radar to the scatter point makes half of the total geocentral angle that is traversed. Therefore, this algorithm is applicable to both bistatic and monostatic configurations.

It is necessary to emphasize that this method fully relies on the availability of accurate elevation angle measurements at the receiver site. Reliable calibration procedures for the SuperDARN interferometry data have been developed in recent years (Ponomarenko et al., 2018; Chisham et al., 2021).

3.2.3 Multistatic Data

On January 10, 2023 we ran a multistatic experiment for 24 hours (from 00:00-23:59 UTC), transmitting from Rankin Inlet at 10.9 MHz and receiving at Rankin Inlet, Inuvik, and Clyde River. This was made possible by GPS-disciplined systems at each site to synchronize within 100 ns between sites. Figure 6 contains a summary plot for beams 7 of Rankin Inlet and Inuvik for this experiment. The left column (panels a, c, e, and g) are plots of conventional monostatic backscattered signals from Rankin Inlet, while the right column (panels b, d, f, and h) are plots of Rankin Inlet signals received at Inuvik. From top to bottom, the rows of panels correspond to the SNR (panels a and b), the Doppler velocity calculated assuming monostatic backscatter at both radars (c, d), the spectral width (e, f), and the elevation angle (g, h). As there exists some persistent signal interference at Rankin Inlet, we removed the isolated pixels with non-physical data. For consistency, the same filtering has been applied to Inuvik data as well. Importantly, Inuvik velocity data shown in this figure were calculated using the conventional SuperDARN monostatic algorithm. For the correct estimation of the velocity magnitude, one must correctly determine the relative location of the scatter point with respect to the transmitter and receiver sites, which will be done later in this subsection.

Inuvik and Rankin Inlet radar sites are located $R_{dir} \simeq 1972$ km apart along the great circle arc. The shortest time for a surface-travelling wave to traverse the distance between sites is $\Delta t_{dir} = 6.58$ ms. We therefore do not expect signals from Rankin Inlet to be detected at $R < R_{dir}$. Indeed, in Figure 6 there are no persistent signals in the bistatic data (right column) received from times of flight Δt less than 6.58 ms. The closest valid data from $\Delta t \simeq 6.6 - 7.3$ ms are characterized by relatively low velocity magnitude and narrow spectral width values ≤ 50 m/s, which satisfy the conventional SuperDARN criteria for ground scatter echoes (see Section 4.1 in Ponomarenko et al., 2007). It means that these echoes most likely are direct signals, i.e., they are likely radar signal reflection by the ionospheric layer rather than scattering by ionospheric irregularities. This mode is equivalent to ground scatter in the monostatic geometry, whose velocity magnitude and spectral width are much smaller than those of the ionospheric scatter. Direct propagation is possible when the skip zone radius is smaller than the distance between the transmitter and receiver, $R_{skip} \leq R_{dir}$. In the monostatic configuration, the skip zone radius can be roughly estimated as a group path to the near edge of the ionospheric scatter and back. This arises from the fact that for the nearly vertical orientation of the geomagnetic field lines, the monostatic backscatter echoes would come approximately from the middle of the respective ground scatter ray trajectory (e.g., the middle of the blue line in Figure 4). From the monostatic data (left column in Figure 6), the near-edge there-and-back time of flight for ionospheric scatter for most of the analyzed 24-hour interval varies within $\Delta t \simeq 2 - 5.5$ ms, which is smaller than Δt_{dir}. Furthermore, as the great circle arc between the two sites lies outside their respective FOVs, the radar signals will be emitted and received through the side lobes of the transmitter (Rankin Inlet) and receiver (Inuvik) antenna arrays, respectively. This can account for the predominantly low SNR of the direct bistatic signals ($\Delta t \simeq 6.6{-}7.3$ ms) observed during this experiment.

The majority of the rest of the bistatic data at $\Delta t \geq 7.3$ ms possess relatively large spectral width and LOS velocity magnitudes that meet the conventional criteria for ionospheric scatter (Ponomarenko et al., 2007). The apparent absence of ground scatter echoes in both bistatic and monostatic data is most likely related to the absence of an effective scatter surface, such as open seawater, within the radar FOVs during the winter months (for more detail see, e.g., Ponomarenko et al., 2010). For bistatic geometry, the closest possible ground scatter range path should be twice that of the skip zone radius, $R \geq 2R_{skip}$, as the radar signal should traverse the ground-ionosphere-ground path twice. It travels first from the transmitter to the ground surface, and then from the ground surface to the receiver.

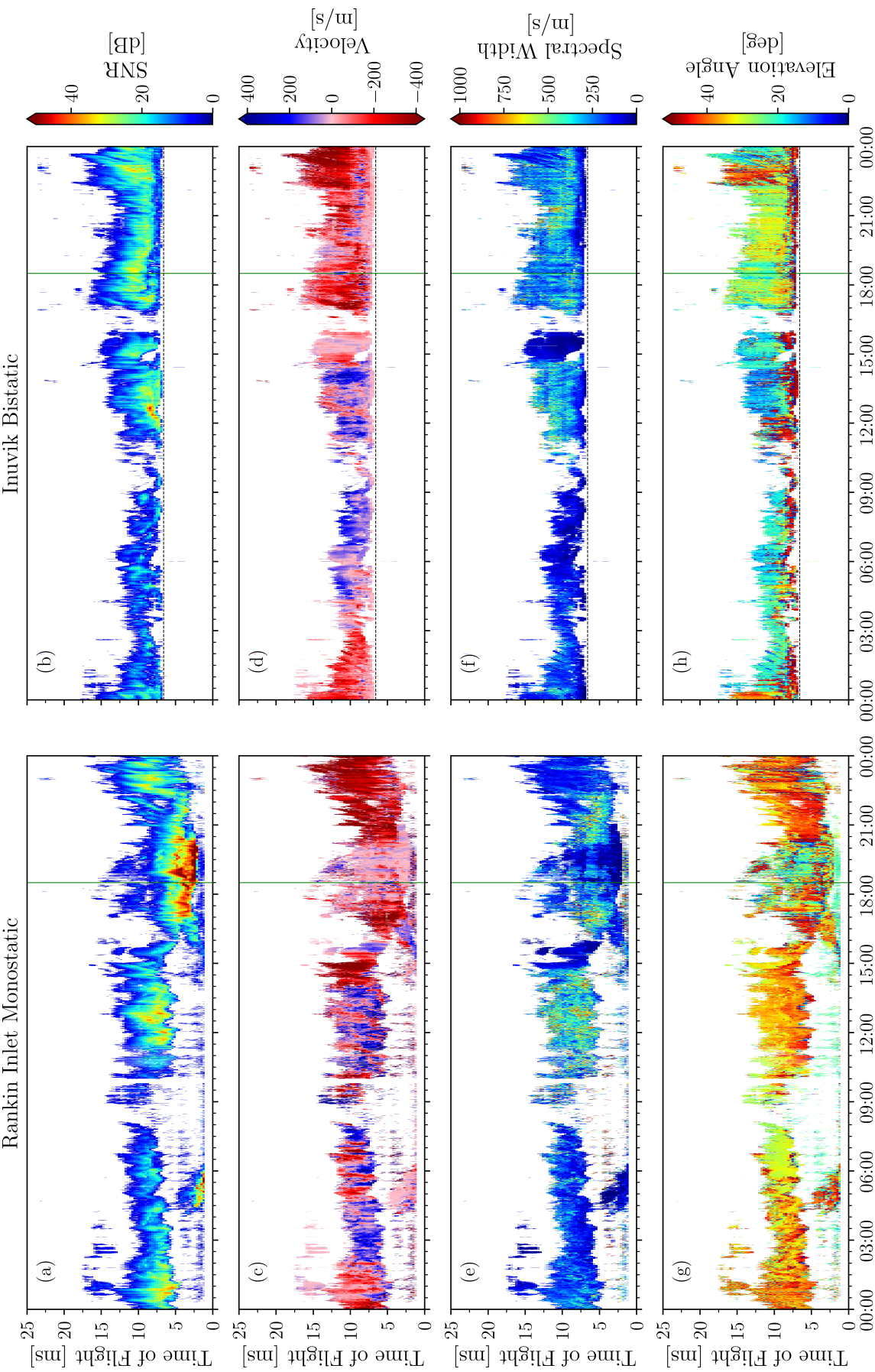

Figure 6: Summary plot for 2023-01-10. The left column shows SNR (a), velocity (c), spectral width (e), and elevation angle (g) for beam 7 of Rankin Inlet which was operating monostatically. The right column shows SNR (b), velocity (d), spectral width (f), and elevation angle (h) for beam 7 of Inuvik, which was operating bistatically and receiving from Rankin Inlet. The horizontal dashed line at $\simeq$ 6.6 ms in the panels of the right column shows the time of flight for the direct path of a surface-travelling wave between Rankin Inlet and Inuvik.

It is important to note that the Doppler shift derived from bistatic operations (Figure 6(d)) does not represent the velocity component along the receiver beam direction, as is the case for a monostatic radar (Figure 6(c)). As discussed in Section 3.2.1, the Doppler shift is imparted by the drift velocity component along the bisector of the transmit and receive beam directions, i.e., along the direction of the line that bisects the angle β in Figure 5(b). Figure 7 contains geolocated data for all three receiver sites for a single integration time of 3.7 seconds beginning at 18:30:00 UTC, which is indicated with vertical green lines in Figure 6. Figures 7(a) and (b) contain SNR and velocity data received by Rankin Inlet operating monostatically. Panels (c-d) and (e-f) contain SNR and velocity of Rankin Inlet emission received at Inuvik and Clyde River, respectively. In the Doppler velocity panels (b, d, f), the scatter locations are indicated by solid dots, and the velocity component direction and magnitude are indicated by the lines extending from each dot. The velocity magnitude and direction are color-coded to assist the reader.

In panel 7(b), the velocity directions are all radially towards or away from the receiving radar, which is expected for the monostatic geometry. In contrast, in panels (d) and (f) the velocity directions are aligned with the bisectors of the transmit and receive directions. The bistatic directions are significantly different from the beam directions for monostatic operations (panel (b)).

An important assumption made in calculating f_D is that the angle θ between $\vec{k}_r$ and $\vec{k}_t$ (see Equation 3) lies in the horizontal plane. In reality, $\vec{k}_r$ and $\vec{k}_t$ can have vertical and horizontal components. As a result, the effective projections of these wave vectors on the horizontal plane are reduced by the factor of $\cos\varepsilon'$, where ε' is the local value of the elevation angle at the scatter point. This leads to an underestimation of the actual velocity component by $(1-\cos\varepsilon')\cdot 100\%$. In our case, ε' inside the ionosphere is always smaller than its value observed from the ground, $\varepsilon' \leq \varepsilon$. Because ionospheric refraction significantly flattens (i.e., bends towards the horizontal plane) the ray trajectories inside the ionosphere, ε' approaches zero in the vicinity of the turning (reflection) point. From Figure 6(h), the receiver elevation angles observed at Inuvik are mostly less than 30°. The median elevation angle value across all 16 beams during 01/10/2023 at group ranges in excess of 7.3 ms is close to 21°, so that the maximum respective error is $(1-\cos 21^\circ)\cdot 100\% \simeq 7\%$. As ε' gets close to ε near the lower ionospheric boundary, where the irregularities of electron density are expected to be weak, the probability of observing echoes with maximum possible velocity distortion $\cos\varepsilon$ is rather low. This will further lower the actual error values to just several percent, which we consider acceptable.

The elevation angle plays an important role in geolocating bistatic echoes. With SuperDARN radars, all signals are assumed to be received from the direction of the peak of the main lobe of the receiver beam. The elevation angle of arriving signals is determined from the phase difference between the main and the interferometer antenna arrays (Milan et al., 1997). If a signal were received from a side lobe, the elevation angle value would be incorrect as its calculation includes a beam direction in the horizontal plane measured from the radar boresight to account for both the change in the effective interferometer base and the conic shape of the linear antenna array beam (e.g., Shepherd, 2017). In testing the geolocation algorithm using real data, we found that the assumptions about signals being received by the main lobe resulted in a number of data points placed behind the receiving radar, which is not a physically correct result for the assumptions made. An apparent position behind the radar is due to signals received from a side lobe. Assuming that these signals coming from the main lobe renders their elevation angles to be incorrectly high. This yields an unphysically small value for Γ in Equation 6 that is smaller than the geocentral angle b between the transmitter and receiver sites. Continuing the geolocation with this incorrect value yields a negative value for the scatterer-to-receiver geocentral angle a. This negative value represents a useful flag to identify signals that were received through side lobes. We also flagged points that had

virtual heights h_{rx} or h_{tx} less than 100 km, as the plasma density at these altitudes is typically too low to generate high-power scatter.

Having identified incorrectly located signals based on the above criteria, we can attempt to correct their geolocation. For all identified signals, we update their nominal beam direction to the first side lobe (usually the next highest-power lobe after the main lobe) and perform the standard SuperDARN elevation angle calculation algorithm in the new direction to find the new elevation angle. With a new elevation angle and beam direction, we perform the bistatic geolocation calculations (Equations 5-8) again. Not all points from side lobes will have originated from the first side lobe, so the process is repeated until either all points are correctly geolocated (i.e., satisfying conditions $a > 0$, $h_{rx}, h_{tx} >$ 100 km) or until we exhaust all side lobes on each side of the main lobe. In the latter case, the data are removed from analysis.

In the bistatic data panels (c-f) in Figure 7, the direct signals identified by short time of flight, i.e., within 600 μs above Δt_{dir} (time equivalent of two range gates), and flagged as ground scatter according to the conventional SuperDARN criteria (Section 4.1 in Ponomarenko et al., 2007) were removed, along with any signals detected unphysically early ($\Delta t < \Delta t_{dir}$). Looking at the SNR measured at Inuvik in panel (c), one can see that the southernmost beams generally exhibit larger SNR than the more northern beams, which makes physical sense due to their closer proximity to the transmitting site. Similarly, in panel (e) the southward beams of Clyde River exhibit higher SNR. Figures 7(c) and 7(e) both show points well outside the conventional FOV determined using the standard (fixed virtual height) geolocation model (e.g., Equations 1 in Chisham et al., 2008). These data were identified as those received through the side lobes of the receiver beams and geolocated accordingly. The bistatic geolocation equations were also applied to monostatic data shown in panels (a) and (b) by merging transmitter and receiver locations (points A and C in Figure 5) but without attributing any points to the side lobes.

Over the 24-hour multistatic experiment, in addition to the monostatic data from Rankin Inlet, a significant amount of data was received simultaneously by the receive-only radars at Inuvik and Clyde River. The total number of geolocated data points recorded by Rankin Inlet was 8385674. At Inuvik and Clyde River, 5809506 and 5379938 data points were recorded, respectively. The combination of monostatic and multistatic data leads to a significant increase in the overall spatial coverage. To demonstrate this, the Northern high-latitude region above 50° geographic latitude was divided into an equal area grid of 1° in latitude and roughly 0.0003 sr in solid angle. This is similar in size to the magnetic coordinate grid used by Ruohoniemi and Baker (1998). Each data point recorded during the multistatic experiment was attributed to one cell in the grid. It is necessary to note that a single grid cell can overlap with several range gates from a single radar. If, during a single integration time, a cell contained at least one valid data point from a given radar, it was counted as a cell with data. An example of such data for a single integration time starting at 18:30:00 UTC is shown in Figure 8. All grid cells containing scatter received by Rankin Inlet operating as a monostatic radar are displayed in panel (a). In panel (b), all scatter from Rankin Inlet (monostatic), as well as Rankin Inlet-Inuvik and Rankin Inlet-Clyde River bistatic links are displayed. The cells in (b) are grouped according to the number of radars that observed scatter in the grid cell during the integration time. It is necessary to emphasize that the standard geolocation model described by Chisham et al. (2008) was developed when accurately calibrated elevation data were not readily available for each radar. This model is based on a set of virtual heights whose values are fixed for each range gate and beam direction. As a result, the standard model produces FOV outlines which are fixed in space and correspond to some average propagation conditions. However, in reality the FOV location and shape vary with changing ionospheric conditions due to variations in ε and, therefore, in virtual height (Equation 5). This means that the actual scatter locations for some data can lay just outside

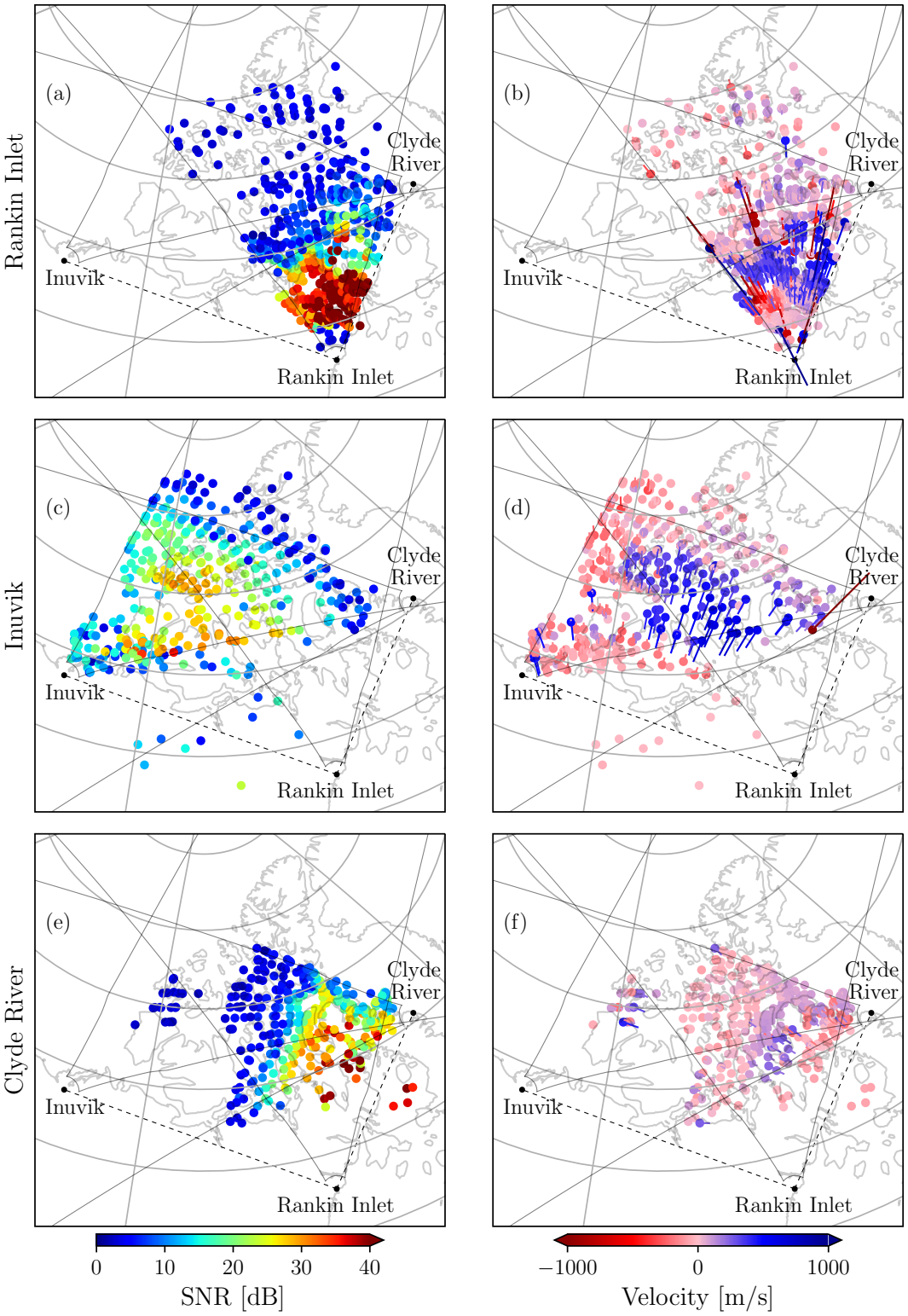

Figure 7: Snapshot of geolocated ionospheric scatter from a single integration time starting at 18:30:00 UTC, showing SNR (left column) and velocity (right column). At this time, Rankin Inlet was the only station transmitting. The top row shows the monostatic data received by Rankin Inlet, while the middle and bottom rows show the bistatic data received by Inuvik and Clyde River radars, respectively. The black dashed lines show the direct paths between Rankin Inlet and the receiver sites at Inuvik and Clyde River.

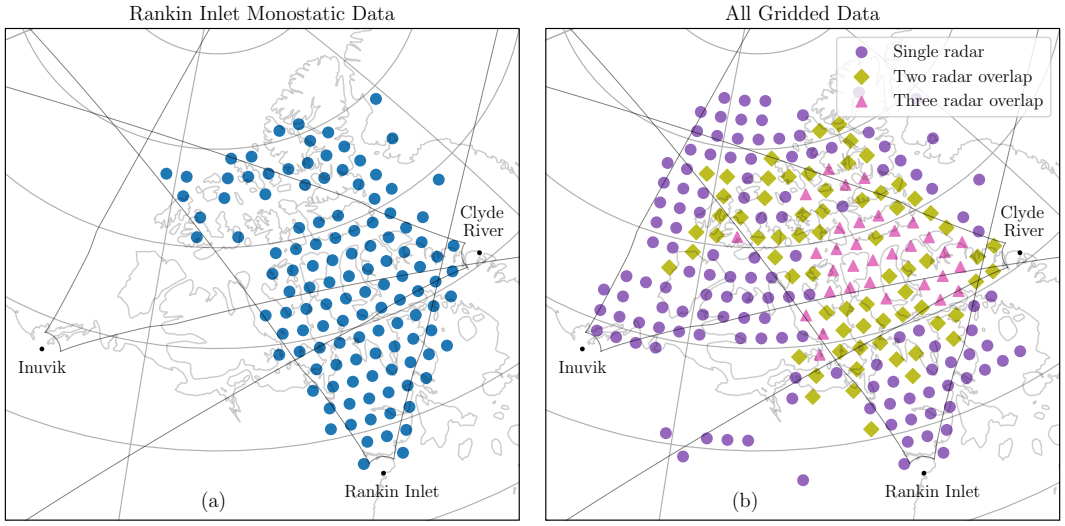

Figure 8: Locations of detected scatter for a single 3.7 second integration time at 18:30:00 UTC. Data for each radar was placed into a 0.0003 steradian equal area geographic grid. Panel (a) contains the scatter collected by Rankin Inlet which was operating monostatically at that time. Panel (b) contains the scatter from Rankin Inlet and bistatic receivers at Inuvik and Clyde River, with grid cells denoted by the number of radars which detected scatter in the cell. Points indicate the geographic center of each cell.

Table 1: Average number of equal area geographic grid cells with ionospheric scatter data per integration time during the multistatic experiment on 10 January 2023. The additional and overlapping data cells and the percentage in brackets are determined with respect to Rankin Inlet data collected in a conventional (monostatic) regime.

Site	Total	Additional	Overlap
Rankin Inlet	85	–	–
Inuvik	107	80 (93%)	27 (31%)
Clyde River	80	35 (41%)	45 (53%)
Inuvik & Clyde River	–	–	21 (25%)

of the conventional FOV boundaries, which can be seen, for example, from the monostatic data in Figure 7 (a, b) and Figure 8(a).

The average numbers of grid cells with data and their percentages with respect to the monostatic data are presented in Table 1. Over the entire 24-hour experiment, inclusion of the Rankin Inlet-Inuvik bistatic link increased the spatial coverage on average by 93%. For the Rankin Inlet-Clyde River link, the increase was 41%. The bistatic data provided a noticeable amount of overlapping data, with Inuvik and Clyde River overlapping with 31% and 53% of the Rankin Inlet data, respectively. The overlapping bistatic velocity measurements allow for the direct calculation of two-dimensional plasma drift velocity vectors for the respective grid cells. Finally, about 25% of the cells with Rankin Inlet data also contained ionospheric scatter data from both Inuvik and Clyde River radars, which additionally allow for an independent estimate of the uncertainty in measuring the full velocity vector.

4 Summary and Future Directions

We developed new operational capabilities for SuperDARN using the recently developed Borealis radar system (McWilliams et al., 2023). We have achieved a 16-fold increase in sampling rate and enabled truly simultaneous measurements across the radar FOV. These advances were implemented using a combination of wide-beam transmission and narrow-beam reception. Using a non-linear phase progression across the antennas in the linear array, we successfully implemented and tested radiation patterns that transmit sufficient power to illuminate the entire conventional SuperDARN FOV. The wide-beam emission provides reliable high-SNR returns across the FOV. Simultaneous reception by multiple narrow beams that are consistent with conventional SuperDARN operations was achieved through post-processing of the data received by each antenna in the radar arrays.

We used the wide-beam transmission to implement multistatic measurements. We transmitted from one radar and received at the transmitter location itself, as well as at two other sites whose FOVs significantly overlap with that of the transmitting radar. Based on commonly used assumptions about HF signal propagation at high latitudes and accurate elevation angle measurements at the receiver sites, we developed a method to determine the geographic coordinates of the footprint of the bistatic echoes. The new geolocation techniques included handling of data received through side lobes. The bistatic geolocation algorithms are applicable to the monostatic configuration as well. Preliminary experiments showed that multistatic operations significantly increases independently measured data points and a considerable extension of spatial coverage compared to monostatic operations. Multistatic operations provided independent LOS velocity measurements that overlapped with $\simeq 30 - 50\%$ of the monostatic velocity data, enabling direct measurements of the full ionospheric plasma drift velocity vectors in these areas.

In the future, we plan to investigate the feasibility of simultaneous wide-beam multistatic measurements in which all Canadian SuperDARN radars, which are equipped with Borealis systems, to transmit at different frequencies. In this mode, the radars with overlapping FOVs will receive both monostatic and multistatic echoes without interfering with each other. This approach can be further extended to each radar transmitting on two or more frequencies simultaneously, while additionally receiving on multiple frequencies from other radars. The validity of the 8-antenna transmission pattern shown in this work is a launching point for simultaneous wide-beam transmission at two frequencies using separate sets of 8 antennas on any one radar.

5 Open Research

The experimental data used in this work will be made publicly available through Zenodo at the time of publication.

Acknowledgments

PP is supported by the Canadian Space Agency (CSA) under grant 21SUSTMRPI. RR is supported by NSERC CGS-M and the University of Saskatchewan. pyDARN (Shi et al., 2022) was used for producing Figures 3 and 6, as well as the individual radar field-of-view outlines in Figures 7 and 8. The authors acknowledge the use of SuperDARN data. SuperDARN is a collection of radars funded by the national scientific funding agencies of Australia, Canada, China, France, Italy, Japan, Norway, South Africa, United Kingdom and United States of America. SuperDARN Canada is supported by the Canada Foundation for Innovation, Innovation Saskatchewan and the Canadian Space Agency.

References

Bendat, J. S., & Piersol, A. G. (2010). *Random data: Analysis and measurement procedures* (4th ed.). John Wiley & Sons, Inc.

Boeringer, D., Werner, D., & Machuga, D. (2005). A simultaneous parameter adaptation scheme for genetic algorithms with application to phased array synthesis. *IEEE Transactions on Antennas and Propagation*, *53*(1), 356-371. doi: 10.1109/TAP.2004.838800

Booker, H., & Gordon, W. (1950). A theory of radio scattering in the troposphere. *Proceedings of the IRE*, *38*(4), 401-412. doi: 10.1109/JRPROC.1950.231435

Booker, H. G. (1956). A theory of scatering by nonisotropic irregularities with application for radar reflections from aurora. *J. Atm. Terr. Phys.*, *8*, 2004–221.

Borisova, T. D., Blagoveshchenska, N. F., Moskvin, I. V., Rietveld, M. T., Kosch, M. J., & Thidé, B. (2002). Doppler shift simulation of scattered HF signals during the Tromsø HF pumping experiment on 16 February 1996. *Annales Geophysicae*, *20*(9), 1479–1486. Retrieved from `https://angeo.copernicus.org/articles/20/1479/2002/` doi: 10.5194/angeo-20-1479-2002

Bristow, W. A., Lyons, L. R., Nishimura, Y., Shepherd, S. G., & Donovan, E. F. (2022). High-Latitude Plasma Convection Based on SuperDARN Observations and the Locally Divergence Free Criterion. *Journal of Geophysical Research: Space Physics*, *127*(12), e2022JA030883. Retrieved from `https://agupubs.onlinelibrary.wiley.com/doi/abs/10.1029/2022JA030883` (e2022JA030883 2022JA030883) doi: https://doi.org/10.1029/2022JA030883

Chisham, G., Burrell, A. G., Marchaudon, A., Shepherd, S. G., Thomas, E. G., & Ponomarenko, P. V. (2021). Comparison of interferometer calibration techniques for improved SuperDARN elevation angles. *Polar Science*, *28*, 100638. Retrieved from `https://www.sciencedirect.com/science/article/pii/S1873965221000025` (SuperDARN / Studies of Geospace Dynamics - Today and Future) doi: https://doi.org/10.1016/j.polar.2021.100638

Chisham, G., Freeman, M. P., & Sofko, G. J. (2008). Mapping ionospheric backscatter measured by the SuperDARN HF radars – Part 1: A new empirical virtual height model. *Ann. Geophys.*, *26*, 823–841, www.ann-geophys.net/26/823/2008/. Retrieved from `https://angeo.copernicus.org/articles/26/823/2008/` doi: https://doi.org/10.5194/angeo-26-823-2008

Chisham, G., Lester, M., Milan, S. E., Freeman, M. P., Bristow, W. A., Grocott, A., ... Walker, A. D. M. (2007). A decade of the Super Dual Auroral Radar Network (SuperDARN): Scientific achievements, new techniques and future directions. *Surv. Geophys.*, *28*, 33–109. doi: 10.1007/s10712-007-9017-8

Cousins, E. D. P., & Shepherd, S. G. (2010). A dynamical model of high-latitude convection derived from SuperDARN plasma drift measurements. *Journal of Geophysical Research: Space Physics*, *115*(A12). Retrieved from `https://agupubs.onlinelibrary.wiley.com/doi/abs/10.1029/2010JA016017` doi: https://doi.org/10.1029/2010JA016017

Davies, K. (1965). *Ionospheric radio propagation.* Washington: National Bureau of standards Monograph 80.

Fiori, R. A. D., Boteler, D. H., Koustov, A. V., Haines, G. V., & Ruohoniemi, J. M. (2010). Spherical cap harmonic analysis of super dual auroral radar network (superdarn) observations for generating maps of ionospheric convection. *Journal of Geophysical Research: Space Physics*, *115*(A7). Retrieved from `https://agupubs.onlinelibrary.wiley.com/doi/abs/10.1029/2009JA015055` doi: https://doi.org/10.1029/2009JA015055

Galushko, V. G., Bezrodny, V. G., Koloskov, A. V., Paznukhov, V. V., & Reinisch, B. W. (2013). Hf wave scattering by field-aligned plasma irregularities considering refraction in the ionosphere. *Radio Science*, *48*(2), 180-189. Retrieved from `https://agupubs.onlinelibrary.wiley.com/doi/abs/10.1029/2012RS005072` doi: https://doi.org/10.1029/2012RS005072

Greenwald, R. A., Baker, K. B., Dudeney, J. R., Pinnock, M., Jones, T. B., Thomas, E. C., ... Yamagishi, H. (1995). DARN/SuperDARN: A global view of the dynamics of high-latitude convection. *Space Sci. Rev.*, *71*, 761-795.

Greenwald, R. A., Baker, K. B., Hutchins, R. A., & Haniuse, C. (1985). An HF phased-array radar for studying small-scale structure in the high-latitude ionosphere. *Radio Sci.*, *20*, 63–79.

Lester, M., Chapman, P. J., Cowley, S. W. H., Crooks, S. J., Davies, J. A., Hamadyk, P., ... Barnes, R. J. (2004). Stereo CUTLASS - A new capability for the SuperDARN HF radars. *Annales Geophysicae*, *22*(2), 459–473. Retrieved from https://angeo.copernicus.org/articles/22/459/2004/ doi: 10.5194/angeo-22-459-2004

McWilliams, K. A., Detwiller, M., Kotyk, K., Krieger, K., Rohel, R., Billett, D. D., ... Ponomarenko, P. (2023). Borealis: An advanced digital hardware and software design for superdarn radar systems. *Radio Science*, *58*(3), e2022RS007591. Retrieved from https://agupubs.onlinelibrary.wiley.com/doi/abs/10.1029/2022RS007591 (e2022RS007591 2022RS007591) doi: https://doi.org/10.1029/2022RS007591

Milan, S. E., Jones, T. B., Robinson, T. R., Thomas, E. C., & Yeoman, T. K. (1997). Interferometric evidence for the observation of ground backscatter originating behind the CUTLASS coherent HF radars. *Annales Geophysicae*, *15*(1), 29–39. doi: 10.1007/s00585-997-0029-y

Nishitani, N., Ruohoniemi, J. M., Lester, M., Baker, J. B. H., Koustov, A. V., Shepherd, S. G., ... others (2019). Review of the accomplishments of mid-latitude Super Dual Auroral Radar Network (SuperDARN) HF radars. *Progress in Earth and Planetary Science*, *6*(27). doi: 10.1186/s40645-019-0270-5

Parris, R. T. (2003). *Design and Implementation of a Meteor Tracking Retrofit System for the Hf Radar at Kodiak Island, Alaska* (M.S. thesis, University of Alaska Fairbanks). Retrieved from http://hdl.handle.net/11122/8549

Perry, G. W., James, H. G., Gillies, R. G., Howarth, A., Hussey, G. C., McWilliams, K. A., ... Yau, A. W. (2017). First results of HF radio science with e-POP RRI and SuperDARN. *Radio Science*, *52*(1), 78-93. Retrieved from https://agupubs.onlinelibrary.wiley.com/doi/abs/10.1002/2016RS006142 doi: https://doi.org/10.1002/2016RS006142

Ponomarenko, P. V., Bland, E. C., McWilliams, K. A., & Nishitani, N. (2022). On the noise estimation in Super Dual Auroral Radar Network data. *Radio Science*, *57*(6), e2022RS007449. Retrieved from https://agupubs.onlinelibrary.wiley.com/doi/abs/10.1029/2022RS007449 (e2022RS007449 2022RS007449) doi: https://doi.org/10.1029/2022RS007449

Ponomarenko, P. V., Maurice, J.-P. S., Hussey, G. C., & Koustov, A. V. (2010). HF ground scatter from the polar cap: Ionospheric propagation and ground surface effects. *Journal of Geophysical Research*, *115*(A10). Retrieved from http://dx.doi.org/10.1029/2010JA015828 (A10310) doi: 10.1029/2010JA015828

Ponomarenko, P. V., St.-Maurice, J.-P., & McWilliams, K. A. (2018). Calibrating HF Radar Elevation Angle Measurements Using E Layer Backscatter Echoes. *Radio Science*, *53*(11), 1438-1449. Retrieved from https://agupubs.onlinelibrary.wiley.com/doi/abs/10.1029/2018RS006638 doi: https://doi.org/10.1029/2018RS006638

Ponomarenko, P. V., & Waters, C. L. (2006). Spectral width of SuperDARN echoes: Measurement, use and physical interpretation. *Ann. Geophys.*, *24*, 115–128. doi: 10.5194/24-115-2006

Ponomarenko, P. V., Waters, C. L., & Menk, F. W. (2007). Factors determining spectral width of HF echoes from high latitudes. *Ann. Geophys.*, *25*, 675-687. doi: 10.5194/angeo-25-675-2007

Ponomarenko, P. V., Waters, C. L., & Menk, F. W. (2008). Effects of mixed scatter

on SuperDARN convection maps. *Annales Geophysicae*, *26*, 1517–1523. doi: 10.5194/angeo-26-1517-2008

Ruohoniemi, J. M., & Baker, K. B. (1998). Large-scale imaging of high-latitude convection with Super Dual Auroral Radar Network HF radar observations. *J. Geophys. Res.*, *103*, 20797-20811.

Shepherd, S. G. (2017). Elevation angle determination for SuperDARN HF radar layouts. *Radio Science*, *52*(8), 938–950. doi: 10.1002/2017RS006348

Shepherd, S. G., Sterne, K. T., Thomas, E. G., Ruohoniemi, J. M., Baker, J. B. H., Parris, R. T., ... Holmes, J. M. (2020). Bistatic observations with SuperDARN HF radars: First results. *Radio Science*, *55*(8), e2020RS007121. doi: https://doi.org/10.1029/2020RS007121

Shi, X., Schmidt, M., Martin, C. J., Billett, D. D., Bland, E., Tholley, F. H., ... McWilliams, K. (2022). pyDARN: A Python software for visualizing SuperDARN radar data. *Frontiers in Astronomy and Space Sciences*, *9*. Retrieved from `https://www.frontiersin.org/articles/10.3389/fspas.2022.1022690` doi: 10.3389/fspas.2022.1022690

Sterne, K. T., Greenwald, R. A., Baker, J. B., & Ruohoniemi, J. M. (2011). Modeling of a twin terminated folded dipole antenna for the Super Dual Auroral Radar Network (SuperDARN). In *2011 IEEE RadarCon (RADAR)* (p. 934-938). doi: 10.1109/RADAR.2011.5960673

SuperDARN Data Analysis Working Group. (2021). *SuperDARN Radar Software Toolkit (version 4.6)* [software]. Zenodo. Retrieved from `https://doi.org/10.5281/zenodo.5156752` (Participating members: Schmidt, M.T., Bland, E.C., Thomas, E.G., Burrell, A.G., Coco, I., Ponomarenko, P. V., Reimer, A.S., Sterne, K.T., and Walach, M.-T.) doi: 10.5281/zenodo.5156752

Thomas, E. G., & Shepherd, S. G. (2018). Statistical patterns of ionospheric convection derived from mid-latitude, high-latitude, and polar superdarn hf radar observations. *Journal of Geophysical Research: Space Physics*, *123*(4), 3196-3216. Retrieved from `https://agupubs.onlinelibrary.wiley.com/doi/abs/10.1002/2018JA025280` doi: https://doi.org/10.1002/2018JA025280

Thomas, E. G., & Shepherd, S. G. (2022). Virtual height characteristics of ionospheric and ground scatter observed by mid-Latitude SuperDARN HF radars. *Radio Science*, *57*(6), e2022RS007429. Retrieved from `https://agupubs.onlinelibrary.wiley.com/doi/abs/10.1029/2022RS007429` (e2022RS007429 2022RS007429) doi: https://doi.org/10.1029/2022RS007429

Willis, N. (2005). Bistatic radar. In (2nd ed., chap. 6). SciTech Publishing Inc.

Yukimatu, A. S., & Tsutsumi, M. (2002). A new SuperDARN meteor wind measurement: Raw time series analysis method and its application to mesopause region dynamics. *Geophys. Res. Lett.*, *29*, 1981, doi:10.1029/2002GL015210.